



# Subglacial bathymetry and sediment distribution beneath Pine Island Glacier ice shelf modeled using aerogravity and in situ geophysical data: New results

Atsuhiro Muto <sup>a,d,\*</sup>, Leo E. Peters <sup>a,1</sup>, Karsten Gohl <sup>b</sup>, Ingo Sasgen <sup>a,c</sup>, Richard B. Alley <sup>a</sup>, Sridhar Anandakrishnan <sup>a</sup>, Kiya L. Riverman <sup>a</sup>

<sup>a</sup> Department of Geosciences the Earth and Environmental Systems Institute, The Pennsylvania State University, University Park, PA 16802, USA

<sup>b</sup> Department of Geosciences, Alfred Wegener Institute Helmholtz-Centre for Polar and Marine Research, Am Alten Hafen 26, 27568 Bremerhaven, Germany

<sup>c</sup> Department of Geodesy and Remote Sensing, GFZ German Research Centre for Geosciences, Telegrafenberg A20, 14473 Potsdam, Germany

<sup>d</sup> Department of Earth and Environmental Science, Temple University, Philadelphia, PA 19122, USA



## ARTICLE INFO

### Article history:

Received 18 May 2015

Received in revised form 16 October 2015

Accepted 20 October 2015

Available online 3 November 2015

Editor: P. Shearer

### Keywords:

Antarctica

sub-ice-shelf bathymetry

subglacial geology

## ABSTRACT

Pine Island Glacier (PIG) in the Amundsen Sea sector of the West Antarctic Ice Sheet (WAIS) is losing mass and contributing to global sea-level rise at an accelerating rate. Although recent observations and modeling have identified the incursion of relatively warm Circumpolar Deep Water (CDW) beneath the PIG ice shelf (PIGIS) as the main driver of this ice-mass loss, the lack of precise bathymetry limits furthering our understanding of the ice-ocean interactions and improving the accuracy of modeling. Here we present updated bathymetry and sediment distribution beneath the PIGIS, modeled by the inversion of aerogravity data with constraints from active-source seismic data, observations from an autonomous underwater vehicle, and the regional gravity-anomaly field derived from satellite gravity observations. Modeled bathymetry shows a submarine ridge beneath the middle of PIGIS that rises ~350 to 400 m above the surrounding sea floor, with a minimum water-column thickness of ~200 m above it. This submarine ridge continues across the whole width of the 45-km wide ice shelf, with no deep troughs crossing it, confirming the general features of the previously predicted sub-ice-shelf ocean circulation. However, the relatively low resolution of the aerogravity data and limitations in our inversion method leave a possibility that there is an undetected, few-kilometers-wide or narrower trough that may alter the predicted sub-ice-shelf ocean circulation. Modeled sediment distribution indicates a sedimentary basin of up to ~800 m thick near the current grounding zone of the main PIG trunk and extending farther inland, and a region seaward of the submarine ridge where sediments are thin or absent with exposed crystalline basement that extends seaward into Pine Island Bay. Therefore, the submarine ridge marks the transition from a thick sedimentary basin providing a smooth interface over which ice could flow easily by sliding or sediment deformation, to a region with no to little sediments and instead a rough interface over which ice flows mainly by deformation. We hypothesize that the post-Last Glacial Maximum retreat of PIG stabilized at this location because of the spatial transition in basal conditions. This in turn supports the hypothesis that the recent retreat of PIG was strongly forced, probably by changes in ocean circulation, rather than occurring because of ongoing response to the end of the ice age or other changes inland of or beneath PIG.

© 2015 Elsevier B.V. All rights reserved.

## 1. Introduction

The Amundsen Sea sector of the West Antarctic Ice Sheet (WAIS) is losing mass at a rate that has more than doubled in the past four decades, and continues to increase (e.g., Mouginot et al., 2014; Sutterley et al., 2014). Pine Island Glacier (PIG), the second largest drainage basin in this sector after Thwaites Glacier

\* Corresponding author at: Department of Earth and Environmental Science, Temple University, Philadelphia, PA 19122, USA.

E-mail address: [amuto@temple.edu](mailto:amuto@temple.edu) (A. Muto).

<sup>1</sup> Now at the Institute for Marine and Antarctic Studies, University of Tasmania, Hobart, Tasmania 7000, Australia.

(TG), has experienced the fastest grounding-line retreat (Rignot et al., 2014), with its discharge increasing more rapidly than that for the larger TG over the last two decades. Through 2010, discharge from PIG equaled or exceeded that from TG, contributing  $\sim 0.12$  mm/yr to sea-level rise (Medley et al., 2014). While TG ice discharge may increase greatly in the future (Joughin et al., 2014), PIG is expected to sustain and perhaps accelerate its mass loss through the 21st century (e.g., Joughin et al., 2010; Gladstone et al., 2012).

The large mass imbalance of PIG is attributed to the incursion of relatively warm Circumpolar Deep Water (CDW) beneath the PIG ice shelf (PIGIS) (e.g., Jenkins et al., 2010; Jacobs et al., 2011; Schmidtko et al., 2014). The resulting increase in melting beneath PIGIS reduced its buttressing effect, leading to an increase in the ice flux from the grounded part of PIG (e.g., Joughin et al., 2010; Pritchard et al., 2012).

Paleoceanographic evidence from the Amundsen Sea suggests that this recent retreat and thinning is anomalous in the context of the Holocene. Grounded ice advanced to near the edge of the continental shelf during the cooling to the last glacial maximum (LGM) ca. 19,000 yr B.P., but retreat to the inner shelf was largely complete by the start of the Holocene ca. 10,000 yr B.P. (e.g., Lowe and Anderson, 2002; Jakobsson et al., 2011; Hillenbrand et al., 2013; Nitsche et al., 2013). Cosmogenic-isotope exposure dating in the Hudson Mountains near PIG shows a rapid ice thinning of more than 100 m at  $\sim 8000$  yr B.P. to near its modern level, with no evidence of additional large or rapid changes until recently (Johnson et al., 2014).

The incursion of warm water beneath PIGIS and elsewhere in the Amundsen Sea Embayment likely resulted from changes in regional wind patterns, in response to some combination of changes in the Antarctic ozone hole, the influence of rising atmospheric concentrations of greenhouse gases, and natural variability in atmospheric circulations (e.g., Joughin et al., 2012; Steig et al., 2012, 2013). Understanding these changes to date, and projecting the evolution of the system, require accurate modeling of oceanic circulation beneath ice shelves.

Although recent observations and modeling have advanced our understanding of ice–ocean interactions beneath PIGIS (e.g., Dutrieux et al., 2014; Stanton et al., 2013), the lack of precise bathymetry limits the accuracy of modeling. Surveys by Autonomous Underwater Vehicle (AUV) (Jenkins et al., 2010) produced high-precision but spatially-limited data. Inversions of aerogravity data provided models of the bathymetry beneath the entire PIGIS (Studinger et al., 2010; Muto et al., 2013a); however, large uncertainties are inevitable because of the limited resolution of the data and inherent non-uniqueness in such an inverse problem.

Since the analysis by Muto et al. (2013a) produced initial results of sub-ice-shelf bathymetry and sediment thickness using NASA's Operation IceBridge (OIB) aerogravity data, important new data have become available. These include active-source seismic data over and near PIGIS as described below, additional OIB aerogravity data, and a new moderate-resolution gravity-field product derived from satellite measurements (Mayer-Gürr et al., 2015) that more accurately characterizes the regional gravity anomaly. We incorporate the new data into an improved inversion for water depth and sediment thickness under and near PIGIS.

## 2. Data and methods

### 2.1. Data

We use the free-air gravity-anomaly data (70-second full wavelength filter) acquired during the 2009–2012 OIB Antarctic campaigns (Cochran and Bell, 2010). OIB data were collected at a nominal aircraft height of approximately 1500 feet (457 m) above

**Table 1**

RMS of crossover differences of free-air gravity anomaly data (in mGals) within and between campaigns. Number of crossover points is indicated by small fonts.

	2009	2010	2011	2012
2009	1.6 207	0.8 22	1.5 134	1.6 54
2010	–	No crossovers	1.8 15	0.4 2
2011	–	–	1.5 40	1.0 5
2012	–	–	–	2.0 10

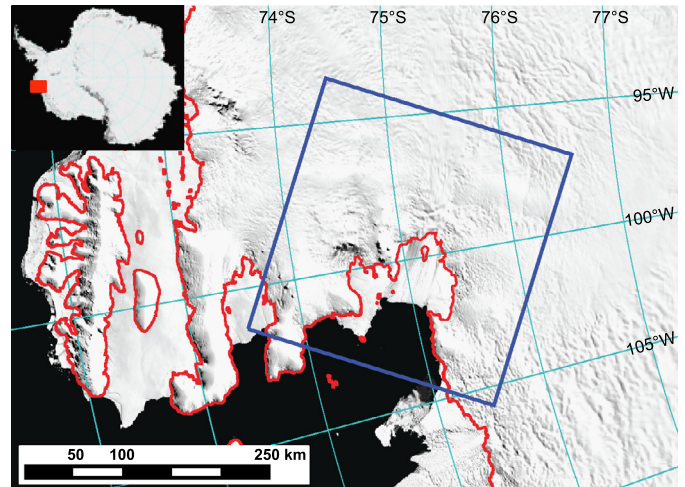


**Fig. 1.** Map indicating the study area (thick blue rectangle). The image is MODIS MOA 2009 (MODIS Mosaic of Antarctica 2008–2009; Haran et al., 2014). Red lines are the grounding line from MEaSUREs (Rignot et al., 2011; Joughin et al., 2010) and Haran et al. (2014). (For interpretation of the references to color in this figure legend, the reader is referred to the web version of this article.)

the surface, which resulted in altitudes of  $\sim 450$ –490 m above the WGS84 ellipsoid over most of the PIGIS, but increased near the fringes of the ice shelf, and exceeded 1500 m towards the ice-sheet interior. We selected the OIB aerogravity data that were collected below an altitude of 1200 m above the WGS84 ellipsoid, and then upward-continued the data from each separate flight line to a constant level of 1200 m using the Taylor-series approximation for upward continuation of uneven surfaces (Blakely, 1995). Since we used data from four different campaigns, we calculated the root mean square (RMS) of crossover differences of the upward-continued data within one campaign and between different campaigns (Table 1). The maximum RMS crossover difference was 2.0 mGal, which we take as the uncertainty in the OIB free-air gravity-anomaly data for this study. We also used the OIB ice and ocean surface elevations measured by the Airborne Topographic Mapper (ATM; Krabill, 2010) and ice thickness derived from the Multi-channel Coherent Radar Depth Sounder (MCoRDS; Leuschen et al., 2010), both of which were obtained concurrently with the aerogravity data. The three data sets were interpolated to a 2.5 by 2.5 km grid covering the area marked by the blue rectangle in Fig. 1. To minimize gridding errors near the edge of the area with upward-continued data, we utilized all of the available OIB gravity data regardless of the campaign and flight altitude in addition to the upward-continued data as explained above. However, we restricted our analyses to areas that are 1) within 2.5 km of an OIB flight line, or within 5 km of two or more flight lines in different directions; and 2) within 2.5 km of both OIB ATM surface elevation and MCoRDS ice thickness observations. Gridded free-air gravity anomaly, ice- and ocean-surface elevations, and ice-bottom depths are in the online Supplementary Material.

We caution readers that the term 'gravity anomaly' may be used differently in geodesy than in geophysics (Hackney and Featherstone, 2003). The 'free-air gravity anomaly' data we used in this study is the 'free-air gravity disturbance' as defined in geodesy

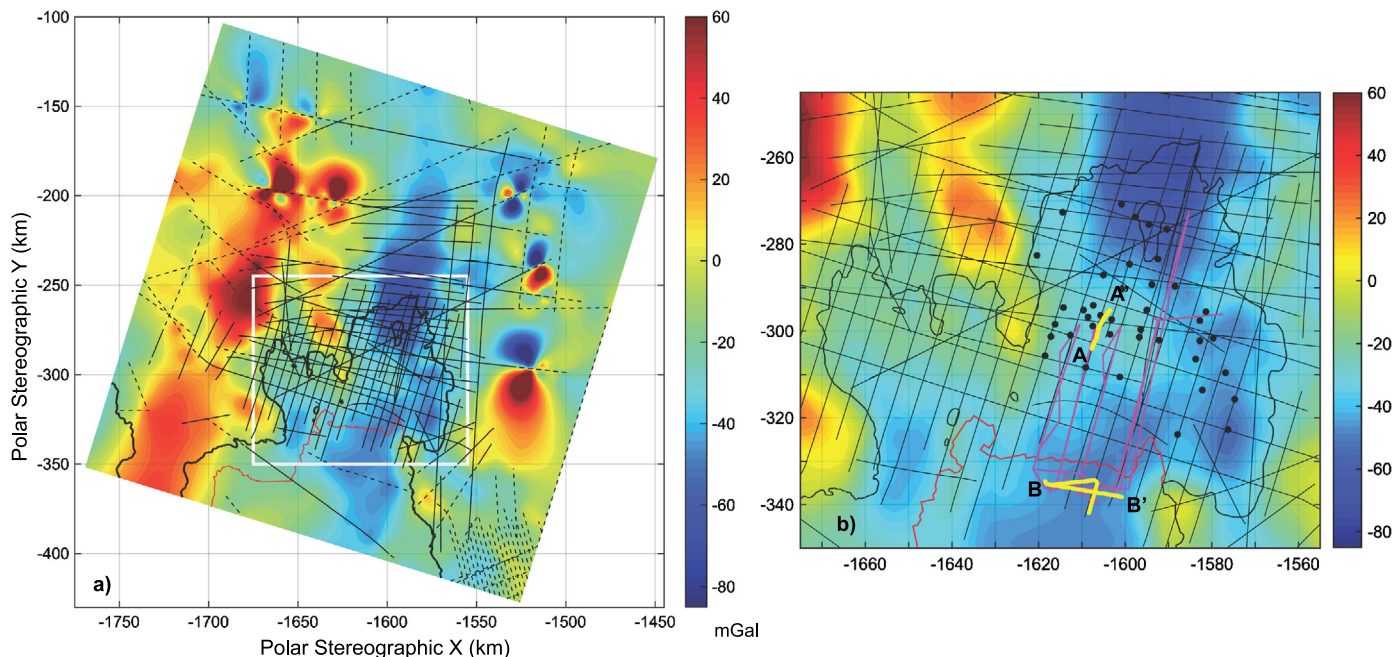


**Fig. 2.** a) Map of gridded Operation IceBridge free-air gravity-anomaly data. Black lines are flight lines with altitude lower than 1200 m above WGS84 ellipsoid and gray lines indicate flight lines used for gridding regardless of flight altitude. Thick black line is the grounding line and thick red line is the edge of the ice shelf visually picked from a MODIS image on November, 9, 2009, obtained from NSIDC's MODIS Antarctic Ice Shelf Image Archive (Scambos et al., 2009). b) Same as a) but zoomed in on the PIG ice shelf. Solid pink lines are the AUV tracks, solid green line is the active-source seismic profile over the PIG ice shelf, solid yellow lines are marine seismic profiles, and black dots are locations of point-source seismic sounding. The map projection used here is the WGS84 Antarctic Polar Stereographic Projection (EPSG reference number 3031) defined in SCAR Antarctic Digital Database Version 6.0 (<http://www.add.scar.org/>). (For interpretation of the references to color in this figure legend, the reader is referred to the web version of this article.)

(Hackney and Featherstone, 2003) since the OIB free-air gravity anomaly is referenced to the WGS84 ellipsoid (Cochran and Bell, 2010). However, we use the term ‘free-air gravity anomaly’ in this paper since that is the name of the distributed data set, and the usage follows numerous geophysical investigations in Antarctica using aerogravity data (e.g., Bell et al., 1998; Jordan et al., 2010).

Seafloor bathymetry beneath the PIGIS has been measured in limited locations by an AUV (Jenkins et al., 2010; solid pink lines in Fig. 2b). Additional observations were made during an active-source reflection-seismic survey (Peters et al., submitted for publication), which constrained the ice bottom and seafloor bathymetry at 41 locations across PIGIS (black dots in Fig. 2b), as well as along a ~10-km long seismic profile (location shown by a solid green line in Fig. 2b, and the seismic section in Fig. 3a). We used the Amundsen Sea bathymetry compilation of Nitsche et al. (2007), combined with the AUV data, to define the seafloor bathymetry of the open ocean. All of these seafloor-depth data were used as fixed constraints in the gravity inversion.

Seismic data also provided constraints on sediment thicknesses in two areas: along the seismic-profile line near the middle of PIGIS as mentioned above, and over open water in front of the ice shelf (location shown by solid yellow lines in Fig. 2b and a seismic section in Fig. 3b). The latter data were collected on a marine multi-channel seismic survey conducted with *R/V Polarstern* in 2010 using a 600-m hydrophone streamer and two GI-Guns (Gohl et al., 2013; Nitsche et al., 2013). These seismic data provided two-way travel times through the well-stratified sedimentary sequences to the top of the underlying basement (Fig. 3b). To derive sediment thicknesses from two-way travel times, we first assumed the density of the sediment (2014 kg/m<sup>3</sup>; see below for justification) and used the density-seismic velocity relation of Nafe and Drake (1963) to estimate the seismic velocity. We then calculated the sediment thicknesses using the estimated seismic velocity and the measured two-way travel times (see Muto et al., 2013b for details).

## 2.2. Regional gravity anomalies

Previous Antarctic aerogravity investigations (e.g., Muto et al., 2013a; Cochran et al., 2014) assumed that the regional gravity anomaly is uniform or varies with a linear trend within a study area. However, our study area, roughly 150 by 150 km, is large enough to be influenced by the gravity anomalies arising from deep geologic sources such as crustal-thickness variations and glacial isostasy, which are unlikely to be uniform or linearly varying. Gravity modeling within ~100 km of our study area (Jordan et al., 2010) indicates that the crust is thin (~20–22 km thick) beneath the main trunk of PIG and thicker to both sides (~24–27 km thick), in response to the rifting inferred to have occurred along the main trunk of PIG, including the area immediately inland of the current grounding zone.

Here, we account for the regional gravity-anomaly field by deriving the long-wavelength Bouguer gravity anomaly using satellite gravity data, and assuming that this Bouguer gravity anomaly mostly reflects the gravity anomaly caused by crustal-thickness variations (Ferraccioli et al., 2011; Bingham et al., 2012). We use the GOCO05S global gravity-field product (Mayer-Gürr et al., 2015), which was derived by combining gravity gradient normal equations from the Gravity field and steady-state Ocean Circulation Explorer (GOCE) and the normal equations of the Gravity Recovery and Climate Experiment (GRACE), based on ITG-GRACE2010s (Mayer-Gürr et al., 2010) according to the approach presented in Pail et al. (2010). The GOCO05S product represents Stokes gravitational potential coefficients up to degree/order 280, which corresponds to spatial resolution of approximately 70 km. We derived the free-air gravity anomaly from GOCO05S for the flight level of 1200 m above the ellipsoid (Petit and Luzum, 2010) in its spherical approximation from the spherical harmonic coefficients (e.g., Heiskanen and Moritz, 1967).

To derive the Bouguer gravity anomaly, we calculated the terrain gravity effect using the ice thickness and bottom depths, and

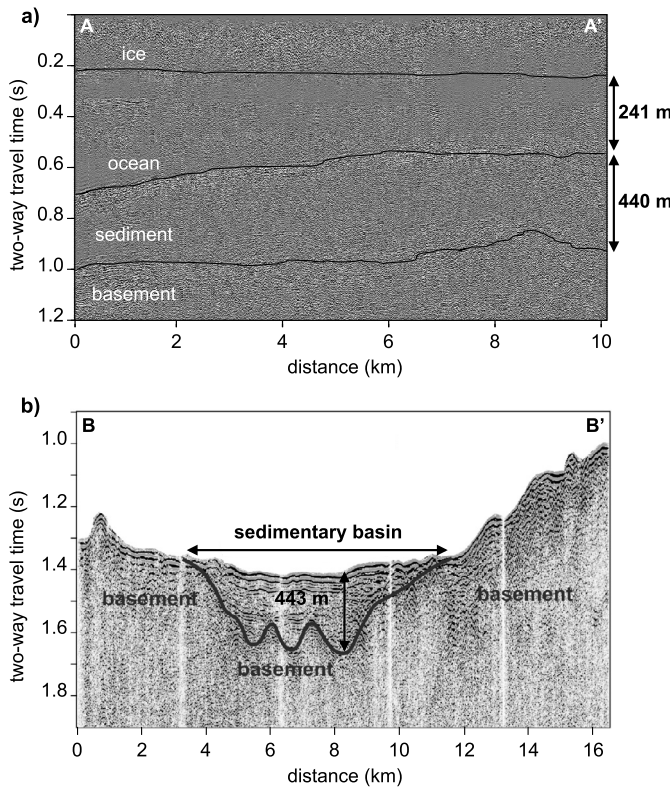


**Fig. 3.** Seismic sections a) in the middle of the PIGIS (solid green line A-A' in Fig. 2b) and b) in front of PIGIS (grid-east-west-striking solid yellow line B-B' in Fig. 2b). Numbers indicate water-column and sediment thicknesses using seismic P-wave velocities of 1459 m/s for ocean water and 2362 m/s for sediments (see text for details on these velocities). Note that these are local thicknesses for the location of the arrows and they differ from thicknesses in the results because of smoothing in the gridding process. (For interpretation of the references to color in this figure legend, the reader is referred to the web version of this article.)

seafloor bathymetry from BEDMAP2 (Fretwell et al., 2013). Since BEDMAP2 includes data from the AUV, the largest gap in measured bathymetry beneath the PIGIS is approximately 30 km, sufficiently small compared to the spatial scale of GOCO05S for our use here. The terrain gravity effect was calculated using the forward method of Plouff (1976) (see Section 2.3, below), with densities of 890 kg/m<sup>3</sup> for ice, 1030 kg/m<sup>3</sup> for ocean water and 2670 kg/m<sup>3</sup> for crust. For this calculation, we used a subsection of BEDMAP2 data 1000 km by 1000 km centered on PIGIS, and subsampled to 4 km resolution to speed up the calculation. The terrain gravity effect was then low-pass filtered to match the wavelength content of GOCO05S. The low-pass filter we used passed wavelengths longer than 110 km, cosine tapered wavelengths between 110 and 70 km, and cut off all wavelengths below 70 km. After several tests with different cut-off-value combinations, we found that 110 and 70 km gave a good match in the power spectra of the terrain gravity effect and the GOCO05S in the wavelength domain. The regional gravity-anomaly field calculated this way is shown in Fig. 4. This regional gravity-anomaly field was then subtracted from the gridded free-air gravity anomaly (Fig. 2) to make the observed gravity-anomaly data for the inversion.

The regional gravity-anomaly field shows higher anomalies along the main trunk of PIG with a local maximum about 50 to 100 km inland of the current grounding zone, and significantly lower anomalies over the Hudson Mountains. These features also are shown in the Bouguer gravity anomaly map of the grounded part of PIG derived from an airborne survey (Jordan et al., 2010) and targeting slightly higher resolution (60 km full wavelength) than our regional gravity-anomaly field. This agreement indicates

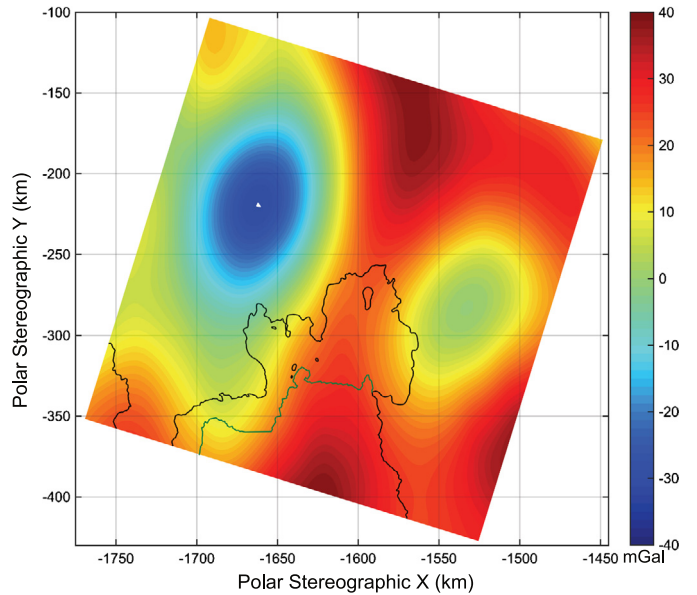


**Fig. 4.** Regional gravity-anomaly map. Solid black line is the grounding line in 2009, and the solid green line is the ice-shelf edge in November 2009. (For interpretation of the references to color in this figure legend, the reader is referred to the web version of this article.)

that gravity anomalies from deep and large-scale geologic features in the PIG region are captured by our regional gravity-anomaly field. The gridded regional gravity-anomaly field is included in the online Supplementary Material.

### 2.3. Gravity inversion

The inversion of the gravity anomalies for bathymetry and sediment-layer thickness was performed with the forward gravity-anomaly calculation method of Plouff (1976). In this method, the domain of interest is discretized into small 3-D rectangular prisms, composed of ice ( $\rho = 890 \text{ kg/m}^3$ ), seawater ( $\rho = 1030 \text{ kg/m}^3$ ) and sediment ( $2014 \text{ kg/m}^3$ , appropriate for rock of a 40% porosity sedimentary matrix filled with seawater) that are on top of crystalline bedrock ( $2670 \text{ kg/m}^3$ ), which is assumed to be a half-space. A sediment layer was included in Muto et al. (2013a) and we continue to do so since active-source seismic surveys detected sediments beneath the PIGIS (Peters et al., submitted for publication), as well as for an area of open water just in front of the ice shelf (Gohl et al., 2013; Nitsche et al., 2013). However, we have no detailed knowledge of the sediment density, and the experimental set-up of the seismic surveys did not allow for the inversion of sediment density; hence, we chose to use the physically reasonable value of  $2014 \text{ kg/m}^3$ , which is consistent with P-wave velocities of the upper 500 m of sediments measured along a seismic refraction line on the middle to outer shelf (Gohl et al., 2013).

The prisms used in the discretization have fixed horizontal dimensions of 2.5 km by 2.5 km. The depth of each layer-interface is allowed to vary, except for ice and water along the AUV tracks and where seismic data are available, and for sediment where the top of basement was detected in the seismic data. The 3-D gravity anomaly of a prism is calculated by the formula of Plouff (1976), and the total gravity anomaly at a given observation point is computed as the sum of the contributions of gravity anomalies from all the prisms. The gravity anomaly for the whole domain is then given by executing the above calculation at all observation points.

Once the gravity anomaly for the whole domain was calculated, we applied a low-pass spatial filter similar to the 70-second full-wavelength line filter used to process OIB data (0% pass at 52.5 s, 100% pass at 105 s full wavelength; Cochran and Bell, 2010) to

match the spatial-frequency content of the observed and calculated anomalies. Assuming a constant aircraft speed of 150 m/s at the time of OIB data collection (Cochran and Bell, 2010), the filter passed wavelengths longer than 15750 m (150 m/s multiplied by 105 s), cosine tapered between 15750 and 7875 m, and cut off all wavelengths below 7875 m.

We included a one-value bulk shift to account for gravity anomalies that may arise from large-scale sources that we did not consider. For example, for the nearby Thwaites Glacier catchment, Damiani et al. (2014) inferred that an upper crust with an assumed density of 2670 kg/m<sup>3</sup> overlies a higher-density lower crust, possibly ~2800 kg/m<sup>3</sup>, and a similar structure could apply to PIG. The bulk shift was calculated as the RMS difference between the observed and calculated gravity anomalies.

We performed our inversion using Very Fast Simulated Annealing (VFSA; Sen and Stoffa, 1995; Roy et al., 2005). We executed five separate runs of VFSA; each run lasted until no new model was accepted for more than 24 hrs. This produced about 7500 models in each run in about 7 days, using Matlab® software and an Intel® Xeon® 2.4 GHz computer. Taking the last 1000 models from each run, we compiled 5000 models in total, and derived the posterior probability density distribution (PPD) of these 5000 models. The mean of the PPD is presented as our most likely model, and the 95% confidence intervals (approximately two standard deviations) are presented as model uncertainties.

The computer code used by Muto et al. (2013a) possessed the following small error. During the model update in each iteration of VFSA, the sediment-layer thickness was erroneously being constrained to larger values in some areas, particularly seaward of the submarine ridge beneath PIGIS. We fixed this error, improving the result for the sediment-layer thickness, as discussed in Section 3. We solve the inverse problem by minimizing the residual function:

$$E = \frac{2 \sum (|g_{obs} - g_{cal}|)}{\sum (|g_{obs} - g_{cal}|) + \sum (|g_{obs} + g_{cal}|)}, \quad (1)$$

where  $g$  is the free-air gravity anomaly, with subscripts  $obs$  and  $cal$  denoting the observed and calculated gravity anomaly, respectively. The normalization in (1) prevents large local anomalies from dominating the inversion through the tendency for larger anomalies to have larger residuals (Roy et al., 2005). Roy et al. (2005) described the option of fitting gravity-anomaly spatial gradients as well as the anomalies themselves, which is useful for recovering geologic features such as faults that create very sharp gravity-anomaly gradients. However, in the absence of knowledge of detailed geologic structures for PIGIS, and because the vertical gradient in the gravity anomaly ( $\delta g/\delta z$  term in the equation for  $E$  in Roy et al., 2005) was not measured by OIB, we chose to fit anomalies and not anomaly gradients. We evaluated the residual function  $E$  for grid points that satisfy the two criteria with regard to the distance from the OIB flight lines and availability of OIB ATM surface elevation and MCoRDS ice thickness data, as explained in Section 2.1.

To speed up the forward calculation of the gravity anomaly, we calculated the gravity effect of only those prisms within a 40-km radius of a particular observation point. In Muto et al. (2013a), this radius was 20 km with the rationale being the gravity effect from prisms farther than 20 km from an observation point was less than one-tenth the magnitude of the uncertainty of the OIB free-air gravity-anomaly data. However, a more rigorous testing of this 20-km calculation radius revealed that in some areas within our study area, the gravity effect of prisms farther away than 20 km exceeds the OIB data uncertainty. We re-evaluated the calculation radius by the following method: we first computed the gravity anomalies in the initial model by increasing the calculation radius to 167 km, equivalent to Hayford zone O (e.g., Dehlinger, 1978), to establish the “correct” gravity anomalies; we then compared these correct anomalies to the anomalies calculated with radii of 20, 30,

40 and 50 km. We found that a radius of at least 40 km is required to reduce the calculation error to less than 2 mGal (uncertainty of the OIB free-air gravity-anomaly data used here) for all points in the domain. A larger radius reduces the calculation error further, but with a substantial increase in the computational time, so we opted to use a 40 km computational radius.

We applied a smoothing filter when perturbing the model, employing a 5:1 weighting of a prism with the eight nearest neighbors in a layer. The VFSA algorithm perturbs the model in a semi-random way in each iteration, which could create models with prisms with unrealistically high and low interface depths next to each other that counteract each other’s gravity effect. The smoothing filter avoids such unnecessarily rough models, and helps in reducing the computational time for convergence to a desired smooth model.

We constrained the extent of grounded ice mainly with the grounding-line position from the NASA MEaSUREs data (Making Earth Science Data Records for Use in Research Environments; Rignot et al., 2011). For the area near the main trunk of PIG where fastest changes in the past ~20 yr have occurred (e.g., Rignot et al., 2014), we used the grounding-line position derived for 2009 by Joughin et al. (2010). We also fixed the sediment-layer thickness to zero for nunataks and domes of the Hudson Mountains, which are eroded inactive volcanoes of wide age range, from 32.8 Ma (Rowley et al., 1990) to as recent as 207 BCE ± 240 yr (Corr and Vaughan, 2008). In addition, we fixed the sediment-layer thickness to zero for small ice rises (isolated grounded ice) indicated by MEaSUREs grounding-line positions, and for grid locations where the grounded ice bottom rises >250 m above the adjacent grids. We assumed these two types of features exist because they consist of resistant bedrock, which is not easily eroded by ice.

### 3. Results and discussion

Figs. 5 and 6 show models of the bathymetry and water-column thickness, and sediment thickness and basement depth, respectively, on the left side, and their 95% confidence intervals or  $2\sigma$  uncertainties on the right side, obtained from the inversion. Areas that do not meet the criteria for inclusion in the residual-evaluation are masked out, as explained in Section 2.3. Figs. 7 and 8 show profiles of the gravity anomalies and cross sections of the model for selected locations shown by black dotted lines in Fig. 6d. Grids of the modeled bathymetry and basement depths, and their  $2\sigma$  uncertainties are available as an online Supplementary Material.

Here, we first discuss the key differences between our new model and the earlier results of Muto et al. (2013a). Secondly, we discuss the residual map (Fig. 9), which, when combined with additional available information such as the bed depth of the grounded ice in BEDMAP2 (Fretwell et al., 2013) and possible errors in OIB MCoRDS ice thickness suggested by another study, provides useful insights on the limitations of our inversion method and the bathymetry at a spatial scale beyond the resolution of the OIB aerogravity data. We then interpret the robust features of the best-fit inversion (Fig. 5a, c, and Fig. 6a, c).

As discussed in Section 2.3, we applied a one-value bulk shift to the entire survey area, to account for the gravity effects of large-scale sources that we did not explicitly consider (e.g., an anomalously dense lower crust). This shift was 1.9 mGal, slightly smaller than the 2 mGal uncertainty of the OIB aerogravity data. In turn, this indicates that the regional gravity-anomaly field derived from GOCO05S sufficiently accounts for any deep-structure gravity signals.

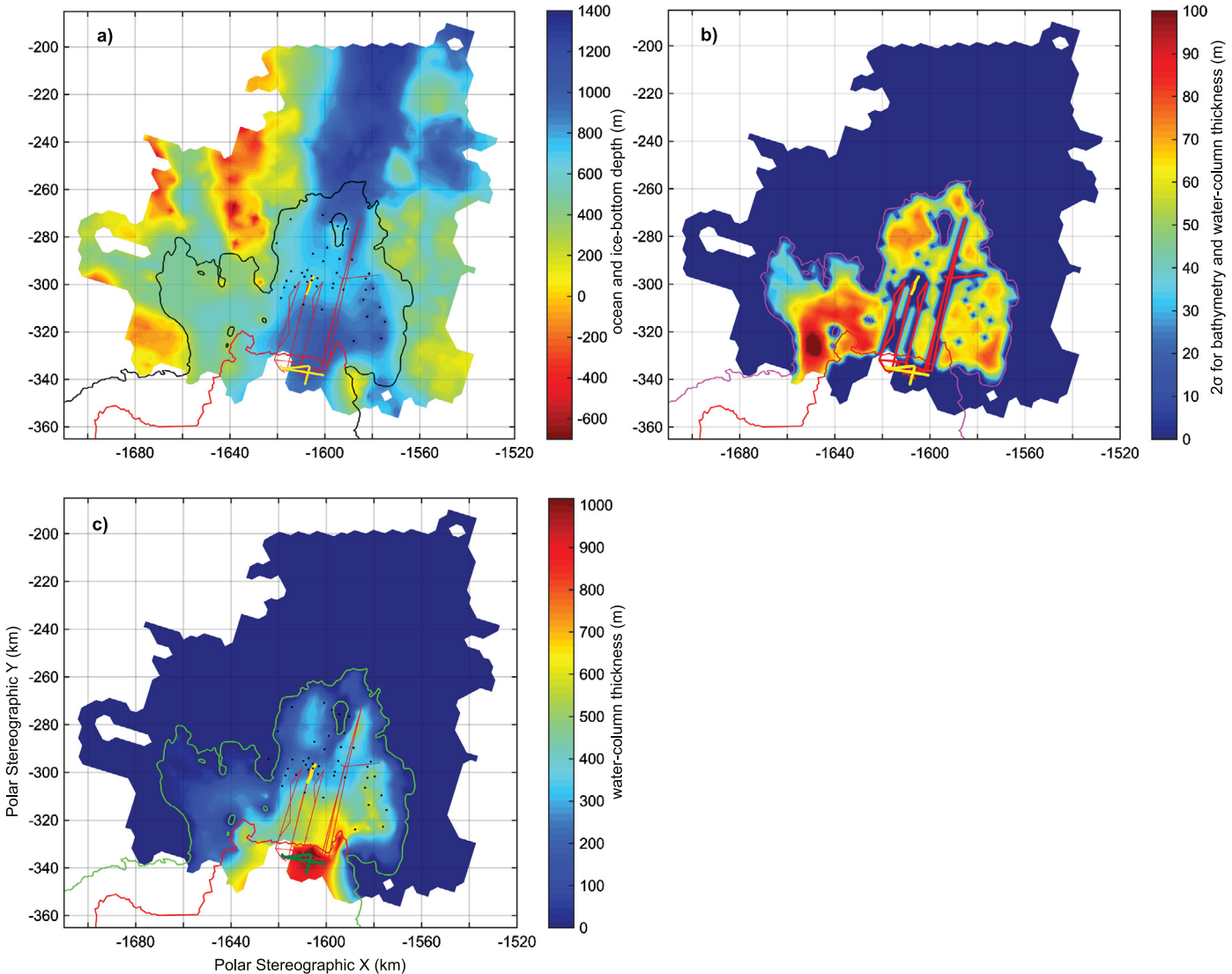


**Fig. 5.** a) The bathymetry with respect to WGS84 ellipsoid modeled from the inversion of OIB aerogravity data, constrained by AUV and active-source seismic data. b)  $2\sigma$  uncertainties for the bathymetry and water-column thickness. c) Water column thickness. Note that  $2\sigma$  uncertainties for the bathymetry and water-column thickness are equal because the ice-bottom depths are constrained by OIB MCoRDS data.

### 3.1. Differences from the previous model in Muto et al. (2013a)

The main features of the new model presented in this study are generally consistent with the results presented in Muto et al. (2013a). The new results cover a larger area, show additional details in some areas arising from the new seismic and OIB data, have greater confidence because of greater computational effort, and have some changes because of correction of the small error in the earlier inversion code.

The most notable improvement is in the sediment thickness. In Muto et al. (2013a), the sediment layer within  $\sim 20$  km seaward of the crest of the submarine ridge is about 200–250 m thick but thickens to  $\sim 500$ –550 m below the edge of the PIGIS and further seaward. The new model shows that seaward of the submarine ridge the sediment is mostly less than  $\sim 150$  m thick, except for the narrow sedimentary basin detected by the marine seismic survey that is up to 380 m thick (Fig. 6a). This key difference primarily arises from the improvement in the computer code, as discussed in Section 2.3, that erroneously constrained the sediment thickness in this area to larger values. The improved map of sediment thickness motivates the new hypothesis with regard to the Holocene stability of PIG, as discussed in Section 3.3.

The modeled bathymetry in this study (Fig. 5a) is very similar to that of Muto et al. (2013a). However, the new results show that the deep basin in the grid-southeastern part of PIGIS seaward of the submarine ridge is generally deeper, typically by  $\sim 100$  m but up to 260 m at the deepest point ( $-1576, -324$ ). The previous estimates were affected by the computational error, but also by the lack of any *in situ* constraints, and were trading off ocean-floor depth and sediment thickness. New seismic spot-sounding data have now constrained the ocean floor to be deeper, thus allowing accurate identification of thinner sediments in the area in the new model.

### 3.2. Insights from residuals

Residuals between the observed gravity anomalies and those calculated from our best-fit inverted model, as shown in Fig. 9, include values in excess of  $\pm 30$  mGal, mostly in the grid-western half (left side in Figs. 5 and 6) of the study area. The residual function  $E$  (equation (1)) for this model is 0.16. The theoretical global minimum residual with the data uncertainty of 2 mGal is 0.04. Some of this difference arises from the computational limitation of finding the global minimum despite using more computational

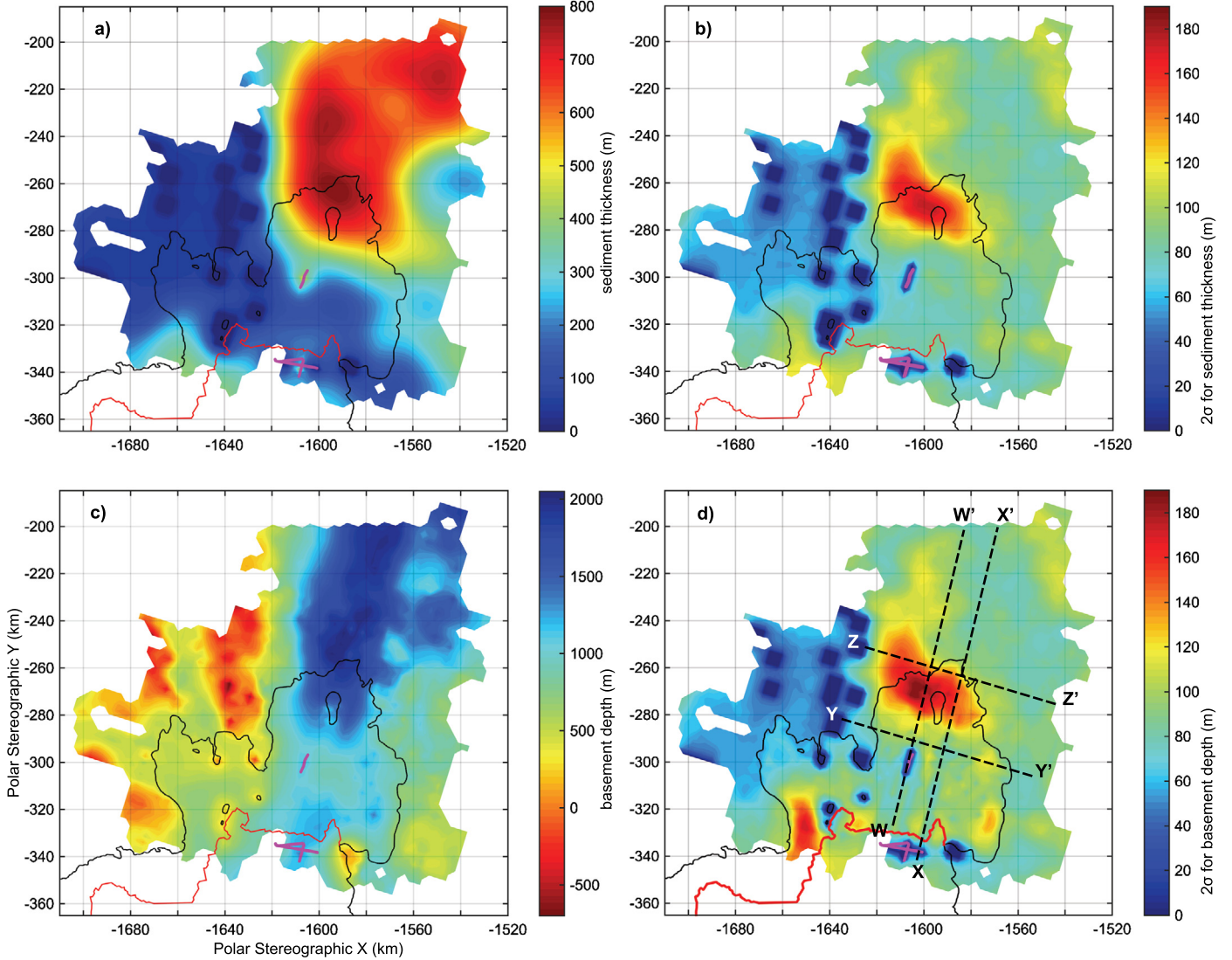


**Fig. 6.** a) The sediment thickness modeled from the inversion of OIB aerogravity data, constrained by active-source seismic data and b) its  $2\sigma$  uncertainty. c) The basement depth with respect to WGS84 ellipsoid and d) its  $2\sigma$  uncertainty. Black dotted lines in d) indicate the locations of 2D profiles shown in Figs. 7 and 8.

resources than in Muto et al. (2013a). Failure to reach the theoretical minimum residual can also arise from our physically motivated constraints, such as matching particular points while enforcing smoothness. Thus, the residual map motivates additional hypotheses, which we discuss briefly before highlighting the main results of the inversion.

The largest-magnitude residuals beneath PIGIS are approximately  $-20$  mGal, seen around the grid southwestern edge of PIGIS in the vicinity of the small ice rises near coordinate  $(-1640, -320)$ . Those likely indicate that the ocean floor is deeper than that returned by the inversion, most likely because the smoothing in the inversion prevented deeper ocean floor very close to the ice rises, which were constrained as grounded. If we manually perturb the inverted model and make the ocean floor deeper by 350 m in this area, the residual remains negative but its magnitude decreases to less than 1 mGal.

Outside of PIGIS, large positive residuals in excess of 30 mGal exist within  $\sim 20$  km of the grid-western edge of the study area (Fig. 9). This area is close to a region where the quoted error in BEDMAP2 bedrock depth is large ( $>370$  m; Fretwell et al., 2013). Our positive residual suggests that the ice is thinner and the bed shallower than in our gridded data, or that the density of basement

underlying the Hudson Mountains is higher than  $2670 \text{ kg/m}^3$ , or a combination of both.

A notable and interesting feature on the residual map (Fig. 9) is the negative residual of approximately 13 mGal centered on an island-like feature of grounded ice in PIGIS at around coordinate  $(-1590, -280)$ . The ice bottom of this feature is 250 to 300 m above the surrounding ocean floor (Fig. 5a). Rignot et al. (2014) noted that this is a region where bed-picking was difficult for MCoRDS, and suggested that the picks were from the apexes of bottom crevasses filled with sea water, whereas the bottom corners of the crevasses marking the true base of PIGIS are 150 to 350 m deeper based on mass-conservation calculations (see their Figure S10). Our result supports this suggestion by Rignot et al. (2014); thicker ice would reduce our modeled gravity anomaly and thus reduce the magnitude of our negative residual. Additional support comes from the seismic constraints of Peters et al. (submitted for publication), who found an ocean-floor depth of 925 m at coordinate  $(-1592, -283)$ , just  $\sim 1$  km from the MCoRDS value of 609 m at coordinate  $(-1593, -283)$ . Thus, our result supports the inference that the sea floor beneath PIGIS along the main trunk of PIG just downflow of the grounding line in 2009 is more

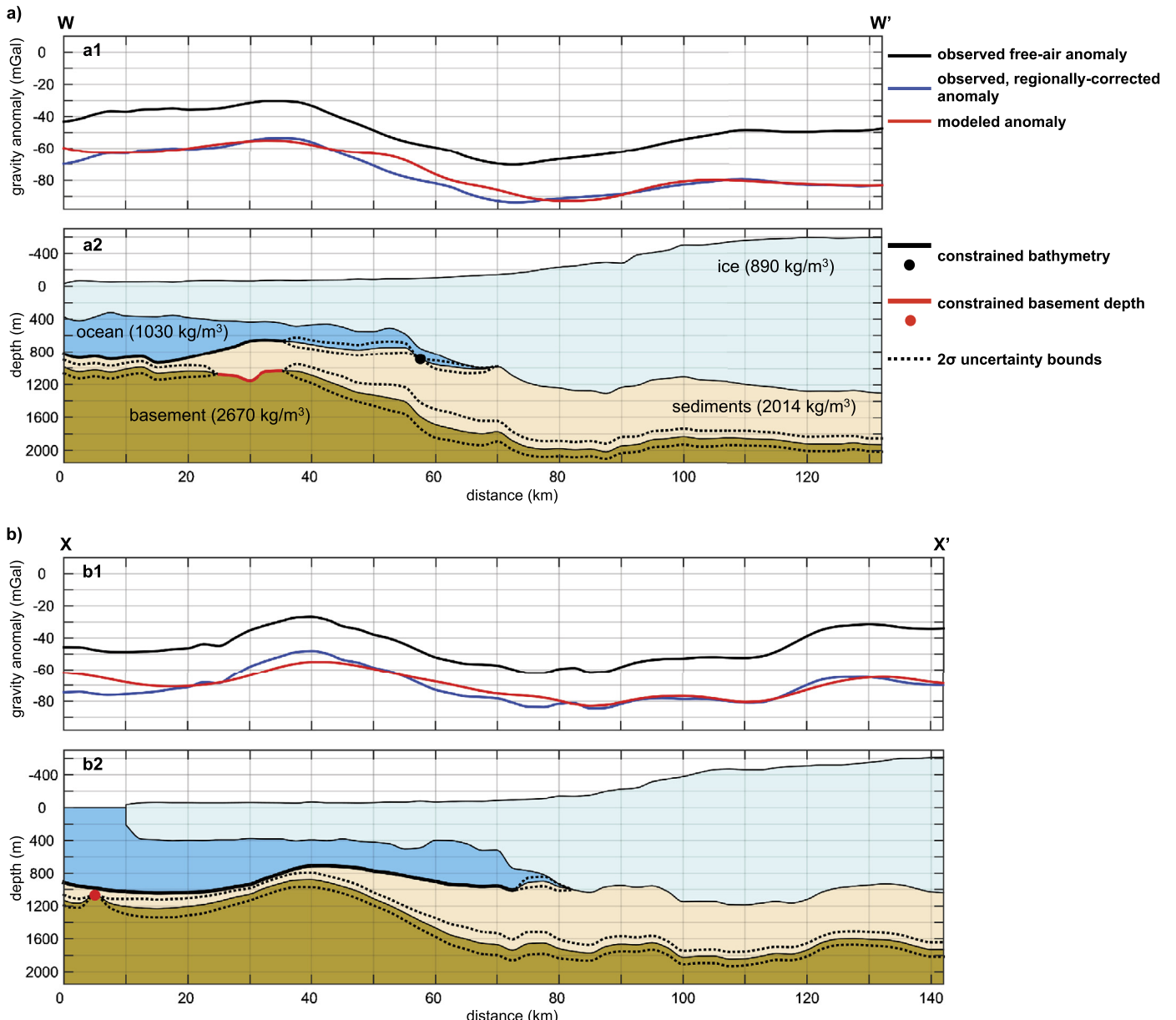


**Fig. 7.** Profiles of gravity anomalies and the model along a) W-W' and b) X-X'. In a1 and b1, the observed (black), observed and regionally-corrected (observed minus regional field; blue) and the modeled (red) gravity anomalies are shown. In a2 and b2, thick solid lines and dots indicate locations where the bathymetry and basement depths are constrained by seismic and/or AUV data, and dotted lines indicate  $2\sigma$  uncertainty bounds for the bathymetry and basement depths. Note that the ice surface and bottom depths are constrained by OIB ATM and MCORDS data. (For interpretation of the references to color in this figure legend, the reader is referred to the web version of this article.)

of a single, smooth basin than the two-lobed feature indicated by the gravity inversion tied to MCORDS (Fig. 5a).

We also find an area with residuals as much as  $-9$  mGal, centered around  $(-1574, -297)$ . This corresponds to the grid-southeastern edge of the submarine ridge, where Peters et al. (submitted for publication) showed a steep deepening (about 300 m in 3 km) of the ocean floor. The gravity-modeled bathymetry for this relatively small area did not fully capture kilometer-scale variations in the ocean-floor depth, mostly due to the smoothness constraint. However, if we manually perturb the modeled bathymetry and make the ocean floor deeper by 300 m as Peters et al. (submitted for publication) showed with seismic and AUV data, the magnitude of residuals decreases to less than 2 mGal. Therefore, our result is consistent with that of Peters et al. (submitted for publication).

### 3.3. Features of the PIG area

Figs. 5a, c, and 6a show our best model of the bathymetry, and water-column and sediment thicknesses. Although there are caveats discussed in the previous section, there are robust features of the PIG region that have important glaciological and oceanographic implications. We discuss some of the highlights next.

The submarine ridge below the main trunk of PIG, originally found by the AUV survey (Jenkins et al., 2010), appears to continue all the way across the width of the  $\sim 45$ -km wide ice shelf, with only a slight deepening of  $\sim 40$  m near coordinate  $(-1590, -295)$  and no major deep troughs crossing it. There is a data-coverage gap (from AUV) of approximately 10 km to grid-northeast between the grounding line and the end of the AUV survey line extending grid-eastward around coordinate  $(-1575, -294)$ , where the

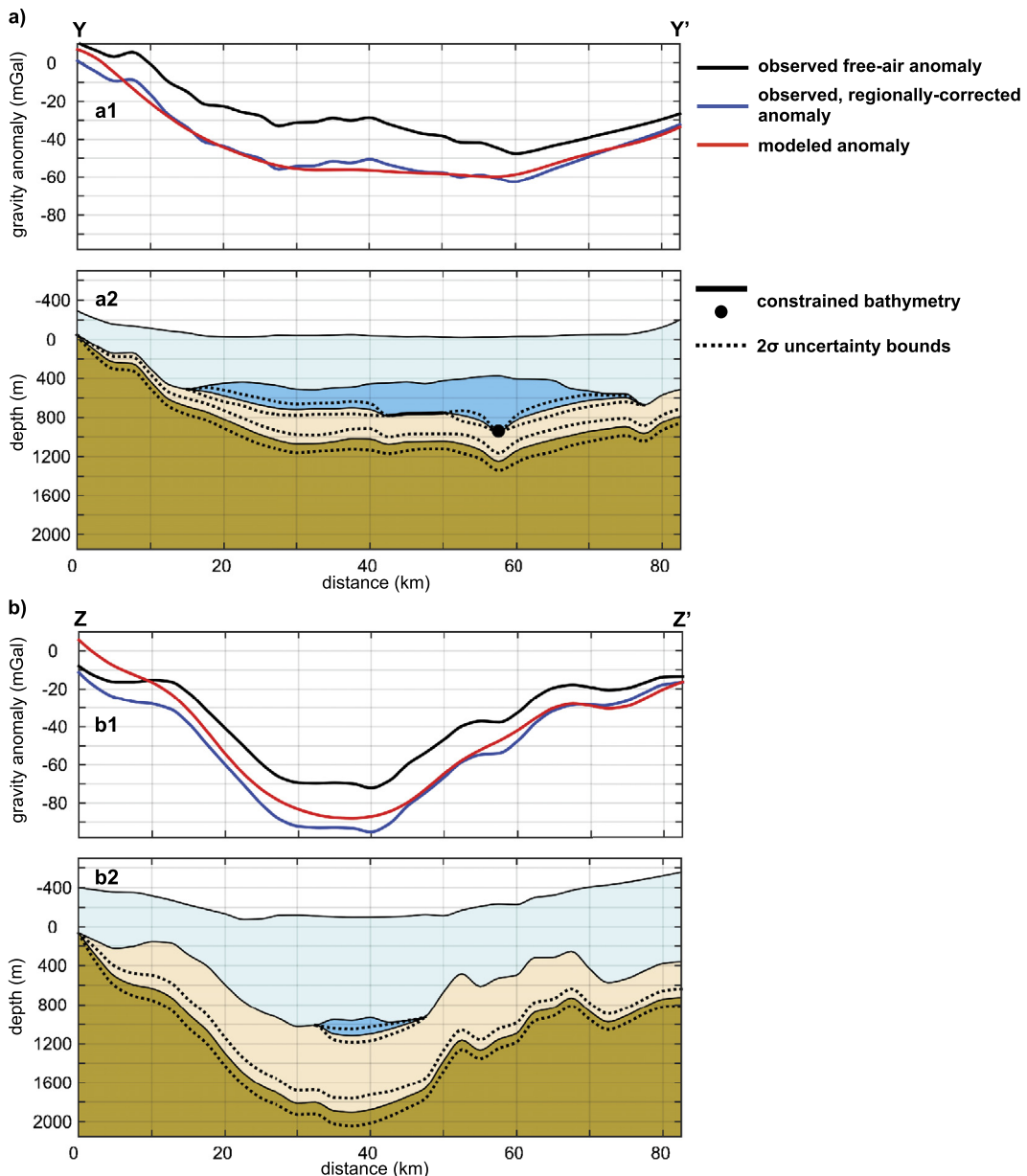


**Fig. 8.** Profiles of gravity anomalies and the model along a) Y-Y' and b) Z-Z'. In a1 and b1, the observed (black), observed and regionally-corrected (observed minus regional field; blue) and the modeled (red) gravity anomalies are shown. In a2 and b2, thick solid lines and dots indicate locations where the bathymetry and basement depths are constrained by seismic and/or AUV data, and dotted lines indicate  $2\sigma$  uncertainty bounds for the bathymetry and basement depths. (For interpretation of the references to color in this figure legend, the reader is referred to the web version of this article.)

inversion result shows the ocean floor getting shallower towards the grounded ice. Because this gap is about the same length as the resolution of OIB gravity-anomaly data, we cannot totally rule out the possibility that a trough less than 10 km wide crosses the ridge there, but we consider this to be unlikely; residuals between the modeled and observed gravity anomaly for this area are mostly less than  $\pm 2$  mGal, with the maximum value of +6 mGal in a small area centered at coordinate ( $-1581, -292$ ), so the most natural interpretation is that the ridge continues across the embayment. We remind readers that the sea floor deepens steeply to the grid-southeast of the submarine ridge and the end of the AUV line, as discussed in the previous section. Nevertheless, we infer that the submarine ridge continues in grid-northeastern direction to the area of grounded ice. Thus, our model of the bathymetry for this previously uncharted part appears to be consistent with the assumed bathymetry used by Dutrieux et al. (2014) in modeling the sub-ice-shelf ocean circulation.

The deep basin in the grid-southeastern part of PIGIS seaward of the submarine ridge is ~900 to 1100 m deep, and as deep as 1160 m at one location ( $-1576, -322$ ) measured by the seismic survey. This deep basin connects grid-westward to another deep basin (1100 m sea-floor depth surveyed by AUV near the coordinate ( $-1590, -325$ )), which provides access for CDW to the interior basin of the PIGIS over the transverse submarine ridge (Dutrieux et al., 2014).

We also note that this extensive and deep grid-southeastern basin appears to be connected to the trough of the grid-northwestward flowing tributary of PIG, referred to as "SW tributary" by MacGregor et al. (2012), although there is a slight bump between the basin and the trough. This suggests the hypothesis that at least part of this basin was eroded by the SW tributary of PIG when it was grounded farther grid northward sometime in the past.

The thin or zero sediment thickness indicated seaward of the submarine ridge beneath the PIGIS is consistent with observations

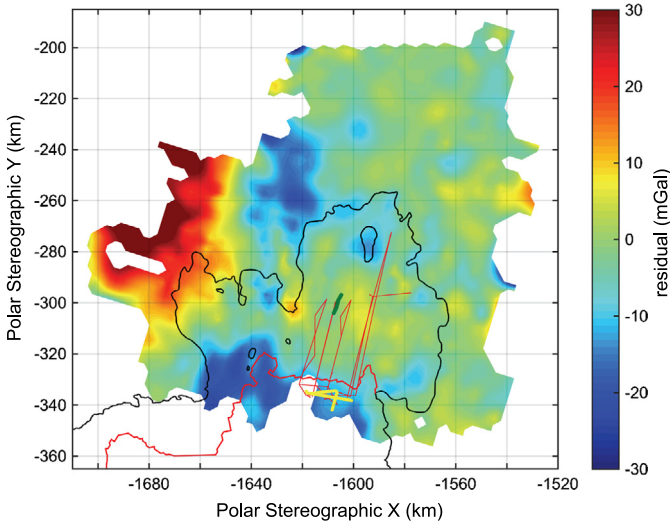


**Fig. 9.** Residuals between the observed and calculated gravity anomalies.

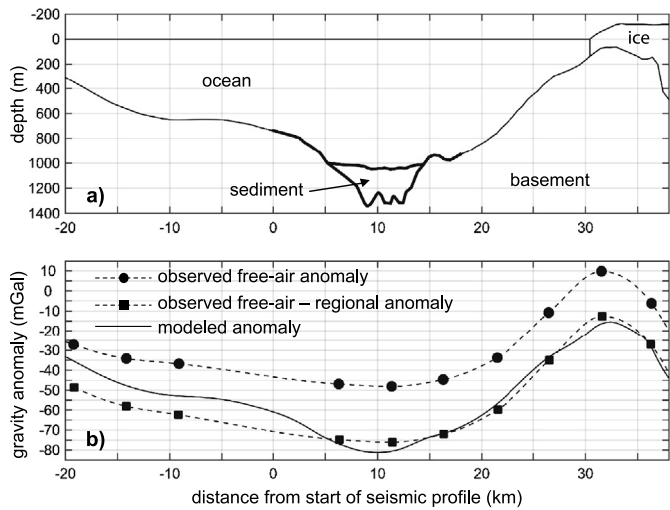


**Fig. 10.** a) Two-dimensional profile of ice, ocean, sediment and bedrock. A section of ocean and sediment floors shown in thick black lines are those measured by the marine seismic survey. b) Gravity-anomaly profiles measured by OIB (dash-circle line), regionally corrected observed gravity anomaly (dash-square line) and modeled from structures shown in a) (solid black line).

of exposed crystalline bedrock on the innermost part of the continental shelf of Pine Island Bay (e.g., Lowe and Anderson, 2003; area 3 in Nitsche et al., 2013; Gohl et al., 2013). Marine surveys show that the exposed bedrock has basins and channels roughly aligned with the direction of inferred paleo-ice stream flow with some sediment infill (e.g., Lowe and Anderson, 2002; Uenzelmann-Neben et al., 2007; Nitsche et al., 2013), but such features are below the resolution of OIB gravity-anomaly data.

To illustrate this point, we compare the OIB-interpolated gravity anomalies along the grid-east-west-striking seismic line (B-B' in Fig. 3b) and its extension, and the expected gravity anomalies at 490 m above WGS84 ellipsoid (average OIB flight altitude for survey lines immediately above the AWI seismic line) from measured bathymetry and sediment basin geometry, modeled using the 2-D method of Talwani et al. (1959) (Fig. 10b). Here, the modeled gravity anomalies are shifted by 9 mGal to align with the observed, regionally-corrected anomalies near the edge of the sedimentary basin. The modeled gravity anomalies show a drop of approximately 5 mGal compared to the measured free-air anomalies across the sedimentary basin, which is not well-resolved in

the data. In part, this may arise from the need to interpolate between OIB flights, as none are collocated with the B-B' seismic line. Also, the 9.2 km width of the ~200–350 m thick sedimentary basin falls below the quoted resolution of OIB gravity data (~5.2 km half-wavelength; Cochran and Bell, 2010). Additionally, this sedimentary basin is possibly narrow and elongated along the PIG flow direction, similar to those found further offshore in Pine Island Bay (Nitsche et al., 2013) but of smaller scale. Similar small, narrow sedimentary basins may exist elsewhere surrounded by exposed bedrock, and might be sought where OIB gravity anomalies show plateaus or local lows.

The 10-km-long seismic profile in the middle of PIGIS (Peters et al., submitted for publication) extended downglacier from near the crest of the submarine ridge. The line detected a clear, continuous reflecting horizon below the ocean floor, which was interpreted as the boundary between sediment and crystalline bedrock, with the sediment thickness varying between 300 m and just over 500 m. Our modeled sediment thickness (Fig. 6a) shows that this seismic profile lies on the transition between the no-sediment/sediment-poor environment seaward of the submarine ridge, and thick sediment landward of the submarine ridge.

Our results show that the sediment thickness near the PIG grounding zone is nearly 800 m, and possibly thicker because of the negative residuals in the region (this excludes the area around the island-like grounded ice that was discussed in Section 3.1). The location and extent of this thick sediment cover roughly corresponds to the sedimentary basin inferred by Jordan et al. (2010) from their more-extensive airborne gravity survey. We used a constant, low sediment density of  $\rho = 2014 \text{ kg m}^{-3}$ , but the limited available data from around Antarctica indicate that such densities are generally restricted to shallower layers, with deeper sediments having higher density. For example, measurements on the ANDRILL core from southern McMurdo Sound (Dunbar et al., 2008) show that the density of  $<2014 \text{ kg m}^{-3}$  reaches down to only ~200 m deep, and the density is between 2200 and  $2500 \text{ kg m}^{-3}$  down to about 1100 m. We thus suggest that the grounding zone of PIG overlies a sedimentary basin that is thicker than 800 m, with density increasing with depth.

In the sedimentary basin extending inland from near the current PIG grounding zone, sediments are thickest beneath the ~40-km-wide trunk of PIG and thinner beneath the glacier flanks (Fig. 6a and Fig. 8b2). This configuration is similar to many other glaciers and ice streams in West Antarctica that occupy sediment-filled troughs, such as in a tributary of Kamb Ice Stream (former Ice Stream C; Anandakrishnan et al., 1998; Bell et al., 1998; Peters et al., 2006), along Ferrigno Ice Stream (Bingham et al., 2012), and near the onset of PIG (Smith et al., 2013). By analogy to these, and from physical understanding, it is likely that the streaming flow of PIG is facilitated by low-density sediments that provide a soft, smooth bed with low basal drag for the majority of the ice stream's length.

We note, however, that our model does show low-density sediments extending outside of the glacier margin including beneath the channel-flanking subglacial topographic highs (Fig. 5a and Fig. 8b2), with more sediments beneath the slower moving ice than in some other settings. For example, Smith et al. (2013) modeled the onset region of PIG as overlying a mix of lower density ( $1900 \text{ kg/m}^3$ ) and higher-density, lithified ( $2400 \text{ kg/m}^3$ ) sediments that pinch out outside of the glacier margin. Similarly, seismic data from Anandakrishnan et al. (1998) show that an upglacier tributary of Kamb Ice Stream overlies ~1000 m of sediment, with a less-consolidated upper layer (~ $2000 \text{ m/s}$  seismic velocity) overlying more-consolidated sedimentary rock, but that both thin to a combined thickness of less than ~200 m coincident with the shear margin and then pinch out within 5 km outboard of the margin. We did not include a higher-density, higher-seismic-velocity layer

of deeper sediments in our gravity inversion because data are not available to constrain it. However, we consider it possible that low-density, soft and easily eroded sediments are restricted to the main trunk of PIG, flanked by a thicker layer of more-lithified sediments than indicated in our preferred model. Alternatively, the flanks of PIG may include basement rock that is lower in density than in our model, but still difficult to erode (Bell et al., 1998).

Important geological control on ice-sheet behavior is suggested by the confirmation here that post-LGM retreat stabilized near the transition from downstream hard bedrock to upstream sedimentary basins. The sediments in basins are likely poorly consolidated marine or glaciomarine deposits, as discussed above, which usually result in smooth surfaces (e.g., Lowe and Anderson, 2002) and erode easily to generate deformable tills. In contrast, subglacial bedrock erosion usually results in rough beds that may later be mantled by often-discontinuous till transported from upstream. Ice flow over rough beds is generally by deformation of the basal layer, and so increases as a low power of the basal shear stress (e.g., Weertman, 1957), whereas flow over smooth till beds may increase with a high power of the basal shear stress approaching perfect plasticity (e.g., Tulaczyk, 2006; Rathbun et al., 2008). When a warming ocean reduces ice-shelf buttressing, a more-nearly viscous bed causes faster ice-sheet flow to be localized just inland, generating relatively large localized thinning and thus favoring grounding-line retreat; in contrast, a more-nearly plastic bed extends the response far inland, limiting the near-coastal thinning that causes grounding-line retreat (Parizek et al., 2013; Alley et al., 2015).

Clearly, grounding lines do retreat across smooth till beds; the nature of the bed influences but does not control grounding-line stability. But, the observed long-term stability of the PIG grounding line near the upstream end of the scoured bedrock, as discussed above, does suggest geologic control, in turn suggesting that the recent retreat was strongly forced. This hypothesis can be tested with modeling that resolves the along-flow variations in basal character, and refined by targeted geophysical studies to further characterize the bed roughness and till distributions.

#### 4. Conclusion

We present up-to-date bathymetry and sediment distribution beneath Pine Island Glacier ice shelf, modeled by inversion of the Operation IceBridge aerogravity data with constraints from *in situ* active-source seismic and AUV data, and the regional gravity anomaly derived from satellite gravity observations. Modeled bathymetry suggests that the submarine ridge below the main trunk of PIG continues across the width of the ice shelf, with no major deep troughs crossing it, consistent with previously predicted sub-ice-shelf ocean circulation. We note, however, that the relatively low resolution of the aerogravity data and limitations in our inversion method leave a slight possibility that there is an undetected narrow trough that may alter this predicted sub-ice-shelf ocean circulation.

The submarine ridge beneath the middle of PIGIS marks the transition from a thick sedimentary basin (soft, smooth bed for ice flow) around the 2009 grounding line beneath the main PIG trunk to a region where sediments thin or do not exist with exposed crystalline basement (rough, resistant bed for ice flow) extending about 200 km seaward into Pine Island Bay. This must have caused a marked change in basal conditions for PIG during the retreat of its grounding line from the ice-age maximum. We hypothesize that this contrast in basal conditions may have caused the PIG grounding line to stabilize near this geological boundary through much of the Holocene, which in turn suggests a strong forcing on the recent rapid PIG grounding-line retreat and ice-mass loss, likely

from oceanic changes as indicated by independent evidence (e.g., Jougin et al., 2012).

Our results reveal subglacial bathymetry and shallow geology on the scale of ~10 km and larger. However, the resolution of the OIB aerogravity data limits us in resolving kilometer-scale features such as exact shapes and depths of narrow troughs in the ocean floor, and sedimentary basins that have been imaged by ship-borne observations. Also, the bulk sediment density we used is a rough estimate; additional data on variation of density with depth would allow more accurate inversion of the gravity data. Pending such additional geophysical and oceanographic surveys, however, we believe our results provide the most up-to-date boundary conditions for coupled ice-ocean modeling of Pine Island Glacier and its ice shelf.

#### Acknowledgements

We thank Adrian Jenkins, British Antarctic Survey and Natural Environment Research Council of U.K. for the permission to use the AUV data. We also thank Tom Jordan for providing helpful guidance for this study and Eric Rignot for useful discussions. We are indebted to NASA and the personnel involved in the Operation IceBridge, and for their data-collection effort. We thank Fausto Ferraccioli and an anonymous reviewer for constructive comments that improved the manuscript. This research was supported in part by NSF through PLR 0424589 and 0909335 and by NASA through NNX10AI04G. I.S. acknowledges funding through the German Academic Exchange Services (DAAD) grant 91545539 and DFG grant SA1734/4-1.

#### Appendix A. Supplementary material

Supplementary material related to this article can be found online at <http://dx.doi.org/10.1016/j.epsl.2015.10.037>.

#### References

- Alley, R.B., Anandakrishnan, S., Christianson, K., Horgan, H.J., Muto, A., Parizek, B.R., Pollard, D., Walker, R.T., 2015. Oceanic forcing of ice-sheet retreat: West Antarctica and more. *Annu. Rev. Earth Planet. Sci.* 43. <http://dx.doi.org/10.1146/annurev-earth-060614-105344>.
- Anandakrishnan, S., Blankenship, D.D., Alley, R.B., Stoffa, P.L., 1998. Influence of subglacial geology on the position of a West Antarctic ice stream from seismic observations. *Nature* 394, 62–65.
- Bell, R.E., Blankenship, D.D., Finn, C.A., Morse, D.L., Scambos, T.A., Brozena, J.M., Hodge, S.M., 1998. Influence of subglacial geology on the onset of a West Antarctic ice stream from aerogeophysical observations. *Nature* 394, 58–62. <http://dx.doi.org/10.1038/27883>.
- Bingham, R.G., Ferraccioli, F., King, E.C., Larter, R.D., Pritchard, H.D., Smith, A.M., Vaughan, D.G., 2012. Inland thinning of West Antarctic Ice Sheet steered along subglacial rifts. *Nature* 487, 468–471. <http://dx.doi.org/10.1038/nature11292>.
- Blakely, R.J., 1995. *Potential Theory in Gravity and Magnetic Applications*. Cambridge University Press, Cambridge, UK.
- Cochran, J.R., Bell, R.E., 2010. IceBridge Sander AIRGrav L1B Geolocated Free Air Gravity Anomalies, October 16–November 9, 2009, November 6–20, 2010, October 14–November 12, 2011, November 4, 2012. NASA Distributed Active Archive Center at the National Snow and Ice Data Center, Boulder, Colorado, USA. <http://nsidc.org/data/iggrvl1b.html>. Digital media, updated 2014.
- Cochran, J.R., Jacobs, S.S., Tinto, K.J., Bell, R.E., 2014. Bathymetric and oceanic controls on Abbot Ice Shelf thickness and stability. *Cryosphere* 8, 877–889. <http://dx.doi.org/10.5194/tc-8-877-2014>.
- Corr, H.F.J., Vaughan, D.G., 2008. A recent volcanic eruption beneath the West Antarctic ice sheet. *Nat. Geosci.* 1 (2), 122–125. <http://dx.doi.org/10.1038/ngeo106>.
- Damiani, T.M., Jordan, T.A., Ferraccioli, F., Young, D.A., Blankenship, D.D., 2014. Variable crustal thickness beneath Thwaites Glacier revealed from airborne gravimetry, possible implications for geothermal heat flux in West Antarctica. *Earth Planet. Sci. Lett.* 407, 109–122. <http://dx.doi.org/10.1016/j.epsl.2014.09.023>.
- Dehlinger, P., 1978. *Marine Gravity*. Elsevier, Amsterdam.
- Dunbar, G.B., Atkins, C., Magens, D., Niessen, F., ANDRILL-SMS Science Team, 2008. Physical properties of the AND-2A core. *ANDRILL Southern McMurdo Sound Project, Antarctica. Terra Antarct.* 15, 49–56.

- Dutrieux, P., Rydt, J.D., Jenkins, A., Holland, P.R., Ha, H.K., Lee, S.H., Steig, E.J., Ding, Q., Povl Abrahamsen, E., Schröder, M., 2014. Strong sensitivity of Pine Island ice-shelf melting to climate variability. *Science* 343, 174–178. <http://dx.doi.org/10.1126/science.1244341>.
- Ferraccioli, F., Finn, C.A., Jordan, T.A., Bell, R.E., Anderson, L.M., Damaske, D., 2011. East Antarctic rifting triggers uplift of the Gamburtsev Mountains. *Nature* 479, 388–394. <http://dx.doi.org/10.1038/nature10566>.
- Fretwell, P., et al., 2013. Bedmap2: improved ice bed, surface and thickness datasets for Antarctica. *Cryosphere* 7, 375–393. <http://dx.doi.org/10.5194/tc-7-375-2013>.
- Gladstone, R.M., Lee, V., Rougier, J., Payne, A.J., Hellmer, H., Le Brocq, A., Shepherd, A., Edwards, T.L., Gregory, J., Cornford, S.L., 2012. Calibrated prediction of Pine Island Glacier retreat during the 21st and 22nd centuries with a coupled flowline model. *Earth Planet. Sci. Lett.* 333, 191–199. <http://dx.doi.org/10.1016/j.epsl.2012.04.022>.
- Gohl, K., Uenzelmann-Neben, G., Larter, R.D., Hillenbrand, C.-D., Hochmuth, K., Kalberg, T., Weigelt, E., Davy, B., Kuhn, G., Nitsche, F.O., 2013. Seismic stratigraphic record of the Amundsen Sea Embayment shelf from pre-glacial to recent times: evidence for a dynamic West Antarctic ice sheet. *Mar. Geol.* 344, 115–131. <http://dx.doi.org/10.1016/j.margeo.2013.06.011>.
- Hackney, R.I., Featherstone, W.E., 2003. Geodetic versus geophysical perspectives of the gravity anomaly. *Geophys. J. Int.* 154, 35–43. <http://dx.doi.org/10.1046/j.1365-246X.2003.01941.x>.
- Haran, T., Bohlander, J., Scambos, T., Painter, T., Fahnestock, M., 2014. MODIS Mosaic of Antarctica 2008–2009 (MOA2009). Image map. National Snow and Ice Data Center, Boulder, Colorado USA.
- Heiskanen, W.A., Moritz, H., 1967. *Physical Geodesy*. Freeman, San Francisco.
- Hillenbrand, C.-D., Kuhn, G., Smith, J.A., Gohl, K., Graham, A.G.C., Larter, R.D., Klages, J.P., Downey, R., Moreton, S.G., Forwick, M., Vaughan, D.G., 2013. Grounding-line retreat of the west Antarctic ice sheet from inner Pine Island Bay. *Geology* 41, <http://dx.doi.org/10.1130/G33469.1>.
- Jacobs, S.S., Jenkins, A., Giulivi, C.F., Dutrieux, P., 2011. Stronger ocean circulation and increased melting under Pine Island Glacier ice shelf. *Nat. Geosci.* 4 (8), 519–523. <http://dx.doi.org/10.1038/ngeo1188>.
- Jakobsson, M., Anderson, J.B., Nitsche, F., Dowdeswell, J.A., Gyllencreutz, R., Kirchner, N., Mohammad, R., O'Regan, M., Alley, R.B., Anandakrishnan, S., Eriksson, B., Kirchner, A., Fernandez, R., Stolldorf, T., Minzoni, R., Majewski, W., 2011. Geological record of ice shelf break-up and grounding line retreat, Pine Island Bay, West Antarctica. *Geology* 39. <http://dx.doi.org/10.1130/G32153.1>.
- Jenkins, A., Dutrieux, P., Jacobs, S.S., McPhail, S.D., Perrett, J.R., Webb, A.T., White, D., 2010. Observations beneath Pine Island Glacier in West Antarctica and implications for its retreat. *Nat. Geosci.* 3, 468–472. <http://dx.doi.org/10.1038/NGEO890>.
- Johnson, J.S., Bentley, M.J., Smith, J.A., Finkel, R.C., Rood, D.H., Gohl, K., Balco, G., Larter, R.D., Schaefer, J.M., 2014. Rapid thinning of Pine Island Glacier in the early Holocene. *Science* 343, 999–1001. <http://dx.doi.org/10.1126/science.1247385>.
- Jordan, T.A., Ferraccioli, F., Vaughan, D.G., Holt, J.W., Corr, H., Blankenship, D.D., Diehl, T.M., 2010. Aerogravity evidence of a major crustal thinning under the Pine Island Glacier region (West Antarctica). *Bull. Geol. Soc. Am.* 122, 714–726. <http://dx.doi.org/10.1130/B26417.1>.
- Joughin, I., Alley, R.B., Holland, D.M., 2012. Ice-sheet response to oceanic forcing. *Science* 338, 1172–1176. <http://dx.doi.org/10.1126/science.1226481>.
- Joughin, I., Smith, B.E., Holland, D.M., 2010. Sensitivity of 21st century sea level to ocean-induced thinning of Pine Island Glacier, Antarctica. *Geophys. Res. Lett.* 37, L20502. <http://dx.doi.org/10.1029/2010GL044819>.
- Joughin, I., Smith, B.E., Medley, B., 2014. Marine ice sheet collapse potentially under way for the Thwaites Glacier Basin, West Antarctica. *Science* 344, 735–738. <http://dx.doi.org/10.1126/science.1249055>.
- Krabill, W.B., 2010. IceBridge ATM L2 Icessn Elevation, Slope, and Roughness, October 16–November 9, November 6–20, 2010, October 14–November 12, 2011, November 4, 2012. National Snow and Ice Data Center, Boulder, Colorado, USA. Digital media, updated 2014.
- Leuschen, C., Gogineni, P., Rodriguez-Morales, F., Paden, J., Allen, C., 2010. IceBridge MCoRDS L2 Ice Thickness, October 16–November 9, 2009, November 6–20, 2010, October 14–November 12, 2011, November 4, 2012. National Snow and Ice Data Center, Boulder, Colorado, USA. Digital media, updated 2015.
- Lowe, A.L., Anderson, J.B., 2002. Reconstruction of the West Antarctic ice sheet in Pine Island Bay during the Last Glacial Maximum and its subsequent retreat history. *Quat. Sci. Rev.* 21, 1879–1897. [http://dx.doi.org/10.1016/S0277-3791\(02\)00006-9](http://dx.doi.org/10.1016/S0277-3791(02)00006-9).
- Lowe, A.L., Anderson, J.B., 2003. Evidence for abundant subglacial meltwater beneath the paleo-ice sheet in Pine Island Bay, Antarctica. *J. Glaciol.* 49, 125–138.
- MacGregor, J., Catania, G.A., Markowski, M.S., Andrews, A.G., 2012. Widespread rifting and retreat of ice-shelf margins in the eastern Amundsen Sea Embayment between 1972 and 2011. *J. Glaciol.* 58 (209), 458–466. <http://dx.doi.org/10.3189/2012JoG11j262>.
- Mayer-Gürr, T., Eicker, A., Kurtenbach, E., Ilk, K.-H., 2010. ITG-GRACE: global static and temporal gravity field models from GRACE data. In: Flechtnner, F., Gruber, T., Güntner, A., Mandea, M., Rothacher, M., Schöne, T., Wickert, J. (Eds.), *System Earth via Geodetic-Geophysical Space Techniques*, pp. 159–168.
- Mayer-Gürr, T., Pail, R., Gruber, T., Fecher, T., Rexer, M., Schuh, W.-D., Kusche, J., Brockmann, J.-M., Rieser, D., Zehentner, N., Kvas, A., Klinger, B., Baur, O., Höck, E.,
- Krauss, S., Jäggi, A., 2015. The combined satellite gravity field model GOCO05s. Presented at EGU General Assembly 2015, Vienna, 12–17 April.
- Medley, B., Joughin, I., Smith, B.E., Das, S.B., Steig, E.J., Conway, H., Gogineni, S., Lewis, C., Criscitiello, A.S., McConnell, J.R., van den Broeke, M.R., Lenaerts, J.T.M., Bromwich, D.H., Nicolas, J.P., Leuschen, C., 2014. Constraining the recent mass balance of Pine Island and Thwaites glaciers, West Antarctica, with airborne observations of snow accumulation. *Cryosphere* 8, 1375–1392. <http://dx.doi.org/10.5194/tc-8-1375-2014>.
- Mouginot, J., Rignot, E., Scheuchl, B., 2014. Sustained increase in ice discharge from the Amundsen Sea Embayment, West Antarctica. *Geophys. Res. Lett.* 41, 1576–1584. <http://dx.doi.org/10.1002/2013GL059069>. from 1973 to 2013.
- Muto, A., Anandakrishnan, S., Alley, R.B., 2013a. Subglacial bathymetry beneath the Pine Island Glacier ice shelf from airborne gravity, constrained by autonomous underwater vehicle data. *Ann. Glaciol.* 54 (64), 27–32. <http://dx.doi.org/10.3189/2013AoG64A110>.
- Muto, A., Christianson, K., Horgan, H.J., Anandakrishnan, S., Alley, R.B., 2013b. Bathymetry and geological structures beneath the Ross Ice Shelf at the mouth of Whillans Ice Stream, West Antarctica, modeled from ground-based gravity measurements. *J. Geophys. Res., Solid Earth* 118, 4535–4546. <http://dx.doi.org/10.1002/jgrb.50315>.
- Nafe, J.E., Drake, C.L., 1963. Physical properties of marine sediments. In: Hill, M.N. (Ed.), *The Sea*, vol. 3. Interscience, New York, pp. 794–815.
- Nitsche, F.O., Gohl, K., Larter, R., Hillenbrand, C.-D., Kuhn, G., Smith, J., Jacobs, S., Anderson, J., Jakobsson, M., 2013. Paleo ice flow and subglacial meltwater dynamics in Pine Island Bay, West Antarctica. *Cryosphere* 7, 249–262. <http://dx.doi.org/10.5194/tc-7-249-2013>.
- Nitsche, F.O., Jacobs, S.S., Larter, R.D., Gohl, K., 2007. Bathymetry of the Amundsen Sea continental shelf: implications for geology, oceanography, and glaciology. *Geochem. Geophys. Geosyst.* 8. <http://dx.doi.org/10.1029/2007GC001694>.
- Pail, R., Goiginger, H., Schuh, W.-D., Höck, E., Brockmann, J.M., Fecher, T., Gruber, T., Mayer-Gürr, T., Kusche, J., Jäggi, A., Rieser, D., 2010. Combined satellite gravity field model GOCO01S derived from GOCE and GRACE. *Geophys. Res. Lett.* 37, L20314. <http://dx.doi.org/10.1029/2010GL044906>.
- Parizek, B.R., Christianson, K., Anandakrishnan, S., Alley, R.B., Walker, R.T., Edwards, R.A., Wolfe, D.S., Bertini, G.T., Rinehart, S.K., Bindschadler, R.A., Nowicki, S.M.J., 2013. Dynamic (in)stability of Thwaites Glacier, West Antarctica. *J. Geophys. Res., Earth Surf.* 118. <http://dx.doi.org/10.1002/jgrf.20044>.
- Peters, L.E., Anandakrishnan, S., Alley, R.B., Winberry, J.P., Voigt, D.E., Smith, A.M., Morse, D.L., 2006. Subglacial sediments as a control on the onset and location of two Siple Coast ice streams, West Antarctica. *J. Geophys. Res.* 111, B01302. <http://dx.doi.org/10.1029/2005B003766>.
- Peters, L.E., Anandakrishnan, S., Stanton, T.P., Dutrieux, P., Riverman, K.L., Truffer, M., Bindschadler, R.A., Holland, D.M., Jenkins, A., submitted for publication. New bathymetric constraints beneath the Pine Island Glacier Ice Shelf, West Antarctica. *Geophys. Res. Lett.*
- Petit, G., Luzum, B. (Eds.), 2010. IERS Conventions (2010). IERS Technical Note, vol. 36. Verlag des Bundesamts für Kartographie und Geodäsie, Frankfurt am Main, Germany. <http://taip.bipm.org/iers/conv2010>.
- Plouff, D., 1976. Gravity and magnetic fields of polygonal prisms and application to magnetic terrain corrections. *Geophysics* 41, 727–741.
- Pritchard, H.D., Ligtenberg, S.R.M., Fricker, H.A., Vaughan, D.G., van den Broeke, M.R., Padman, L., 2012. Antarctic ice-sheet loss driven by basal melting of ice shelves. *Nature* 484, 502–505. <http://dx.doi.org/10.1038/nature10968>.
- Rathbun, A.P., Marone, C., Alley, R.B., Anandakrishnan, S., 2008. Laboratory study of the frictional rheology of sheared till. *J. Geophys. Res.* 113, F02020. <http://dx.doi.org/10.1029/2007F000815>.
- Rignot, E., Mouginot, J., Morlighem, M., Seroussi, H., Scheuchl, B., 2014. Widespread, rapid grounding line retreat of Pine Island, Thwaites, Smith, and Kohler glaciers, West Antarctica, from 1992 to 2011. *Geophys. Res. Lett.* 41. <http://dx.doi.org/10.1002/2014GL061040>.
- Rignot, E., Mouginot, J., Scheuchl, B., 2011. Antarctic grounding line mapping from differential satellite radar interferometry. *Geophys. Res. Lett.* 38, L10504. <http://dx.doi.org/10.1029/2011GL047109>.
- Rowley, P.D., Laudon, T.S., La Prade, K.E., LeMasurier, W.E., 1990. Hudson Mountains. In: LeMasurier, W., Thomson, J., Baker, P., Kyle, P., Rowley, P., Smellie, J., Verwoerd, W. (Eds.), *Volcanoes of the Antarctic Plate and Southern Oceans*. In: *Antarctic Research Series*, vol. 48. American Geophysical Union, Washington D.C., pp. 289–293.
- Roy, L., Sen, M.K., Blankenship, D.D., Stoffa, P.L., Richter, T.G., 2005. Inversion and uncertainty estimation of gravity data using simulated annealing: an application over Lake Vostok, East Antarctica. *Geophysics* 70 (1), J1–J12. <http://dx.doi.org/10.1190/1.1852777>.
- Scambos, T., Bohlander, J., Raup, B., 2009. Images of Antarctic ice shelves. National Snow and Ice Data Center. Digital Media, Boulder, Colorado, USA. [http://nsidc.org/data/iceshelves\\_images](http://nsidc.org/data/iceshelves_images).
- Schmidtko, S., Heywood, K.J., Thompson, A.F., Aoki, S., 2014. Multidecadal warming of Antarctic waters. *Science* 346, 1227–1231. <http://dx.doi.org/10.1126/science.1256117>.
- Sen, M.K., Stoffa, P.L., 1995. *Global Optimization Methods in Geophysical Inversion. Advances in Exploration Geophysics*, vol. 4. Elsevier, Amsterdam.
- Smith, A.M., Jordan, T.A., Ferraccioli, F., Bingham, R.G., 2013. Influence of subglacial

- conditions on ice stream dynamics: Seismic and potential field data from Pine Island Glacier, West Antarctica. *J. Geophys. Res., Solid Earth* 118, 1471–1482. <http://dx.doi.org/10.1029/2012JB009582>.
- Stanton, T.P., Shaw, W.J., Truffer, M., Corr, H.F.J., Peters, L.E., Riverman, K.L., Bindschadler, R., Holland, D.M., Anandakrishnan, S., 2013. Channelized ice melting in the ocean boundary layer beneath Pine Island Glacier, Antarctica. *Science* 341, 1236–1238. <http://dx.doi.org/10.1126/science.1239373>.
- Steig, E.J., Ding, Q., Battisti, D.S., Jenkins, A., 2012. Tropical forcing of Circumpolar Deep Water inflow and outlet glacier thinning in the Amundsen Sea Embayment, West Antarctica. *Ann. Glaciol.* 53 (60), 19–28. <http://dx.doi.org/10.3189/2012AoG60A110>.
- Steig, E.J., Ding, Q., White, J.W.C., Küttel, M., Rupper, S.B., Neumann, T.A., Neff, P.D., Gallant, A.J.E., Mayewski, P.A., Taylor, K.C., Hoffmann, G., Dixon, D.A., Schoennemann, S.W., Markle, B.R., Fudge, T.J., Schneider, D.P., Schauer, A.J., Teel, R.P., Vaughn, B.H., Burgener, L., Williams, J., Korotkikh, E., 2013. Recent climate and ice-sheet changes in West Antarctica compared with the past 2,000 years. *Nat. Geosci.* 6, 372–375. <http://dx.doi.org/10.1038/ngeo1778>.
- Studinger, M., Allen, C.T., Blake, W., Shi, L., Elieff, S.H., Krabill, W.B., Sonntag, J.G., Martin, S., Dutrieux, P., Jenkins, A., Bell, R.E., 2010. Mapping Pine Island Glacier's sub-ice cavity with airborne gravimetry. Abstract C11A-0528 presented at Fall Meeting 2010, AGU, San Francisco, CA, 13–17 Dec.
- Sutterley, T.C., Velicogna, I., Rignot, E., Mouginot, J., Flament, T., van den Broeke, M.R., van Wessem, J.M., Reijmer, C.H., 2014. Mass loss of the Amundsen Sea Embayment of West Antarctica from four independent techniques. *Geophys. Res. Lett.* <http://dx.doi.org/10.1002/2014GL061940>.
- Talwani, M., Worzel, J., Landisman, M., 1959. Rapid Gravity computations for two-dimensional bodies with application to the Mendocino submarine fracture zone. *J. Geophys. Res.* 64, 49–59.
- Tulaczyk, S., 2006. Scale independence of till rheology. *J. Glaciol.* 52, 377–380. <http://dx.doi.org/10.3189/172756506781828601>.
- Uenzelmann-Neben, G., Gohl, K., Larner, R.D., Schlüter, P., 2007. Differences in ice retreat across Pine Island Bay, West Antarctica, since the Last Glacial Maximum: indications from multichannel seismic reflection data. In: Cooper, A.K., Raymond, C.R., et al. (Eds.), *Proceedings of the 10th ISAES. USGS Open-File Report 2007-1047*.
- Weertman, J., 1957. On the sliding of glaciers. *J. Glaciol.* 3, 33–38.